

A Study on Sulfate Optical Properties and Direct Radiative Forcing Using LASG-IAP General Circulation Model

LI Jiandong^{1,2} (李剑东), Zhian SUN³ (孙治安), LIU Yimin¹ (刘屹岷), Jiangnan LI⁴ (李江南), Wei-Chyung WANG^{*2} (王维强), and WU Guoxiong¹ (吴国雄)

¹*State Key Laboratory of Numerical Modeling for Atmospheric Sciences and Geophysical Fluid Dynamics,*

Institute of Atmospheric Physics, Chinese Academy of Sciences, Beijing 100029

²*Atmospheric Sciences Research Center, State University of New York,*

Albany, New York, USA 12203

³*Center for Australian Weather and Climate Research, Australian Bureau of Meteorology,
Melbourne, Victoria, Australia*

⁴*Canadian Center for Climate Modeling and Analysis, University of Victoria,
Victoria, British Columbia, Canada*

(Received 10 December 2011; revised 14 February 2012)

ABSTRACT

The direct radiative forcing (DRF) of sulfate aerosols depends highly on the atmospheric sulfate loading and the meteorology, both of which undergo strong regional and seasonal variations. Because the optical properties of sulfate aerosols are also sensitive to atmospheric relative humidity, in this study we first examine the scheme for optical properties that considers hydroscopic growth. Next, we investigate the seasonal and regional distributions of sulfate DRF using the sulfate loading simulated from NCAR CAM-Chem together with the meteorology modeled from a spectral atmospheric general circulation model (AGCM) developed by LASG-IAP. The global annual-mean sulfate loading of 3.44 mg m^{-2} is calculated to yield the DRF of -1.03 and -0.57 W m^{-2} for clear-sky and all-sky conditions, respectively. However, much larger values occur on regional bases. For example, the maximum all-sky sulfate DRF over Europe, East Asia, and North America can be up to -4.0 W m^{-2} . The strongest all-sky sulfate DRF occurs in the Northern Hemispheric July, with a hemispheric average of -1.26 W m^{-2} . The study results also indicate that the regional DRF are strongly affected by cloud and relative humidity, which vary considerably among the regions during different seasons. This certainly raises the issue that the biases in model-simulated regional meteorology can introduce biases into the sulfate DRF. Hence, the model processes associated with atmospheric humidity and cloud physics should be modified in great depth to improve the simulations of the LASG-IAP AGCM and to reduce the uncertainty of sulfate direct effects on global and regional climate in these simulations.

Key words: sulfate, optical properties, direct radiative forcing, atmospheric general circulation model

Citation: Li, J. D., Z. A. Sun, Y. M. Liu, J. N. Li, W.-C. Wang, and G. X. Wu, 2012: A study on sulfate optical properties and direct radiative forcing using the LASG-IAP general circulation model. *Adv. Atmos. Sci.*, **29**(6), 1185–1199, doi: 10.1007/s00376-012-1257-y.

1. Introduction

Presently, aerosols are well known as major natural and anthropogenic climate forcing agents, and they

exert significant effects on the Earth's climate (Forster et al., 2007). Aerosols change the radiation budget by directly scattering and absorbing incident radiation. Meanwhile, many kinds of aerosols exist in the atmo-

*Corresponding author: Wei-Chyung WANG, wewang@albany.edu

© China National Committee for International Association of Meteorology and Atmospheric Sciences (IAMAS), Institute of Atmospheric Physics (IAP) and Science Press and Springer-Verlag Berlin Heidelberg 2012

sphere and act as cloud condensation nuclei (CCN) (Twomey, 1977; Albrecht, 1989). In this way, aerosols indirectly modify the microphysical and optical properties of clouds. However, the magnitude of radiative forcing due to aerosols is not accurately known, compared to other anthropogenic sources of climate change (Forster et al., 2007). Aerosols pose significant challenges to current climate models, including the treatment of emissions, transportation and sediment, cloud microphysics, and radiative processes (Ramaswamy et al., 2001). Though climate models to study the Earth's atmospheric system have been in development for several decades, even the most sophisticated models are unable to fully represent all interactive aerosol processes and their effects. Nonetheless, significant progresses have been made in understanding the Earth's climate system and in identifying sources of model uncertainty.

Sulfate is a major scattering aerosol (Kiehl and Briegleb, 1993) and a dominant source of CCN over many regions (Lohmann et al., 1999). Many researchers have examined the direct and indirect effects of sulfate on climate simulations. These studies suggest that sulfate can reflect solar radiation, dimming Earth's surface and thus partly offsetting the warming effect caused by increases in greenhouse gases. Based on current best estimates (Forster et al., 2007), sulfate direct radiative forcing (DRF) is approximately -0.4 W m^{-2} , with an uncertainty of $\pm 0.2 \text{ W m}^{-2}$. For sulfate cloud albedo forcing, it is about -1.3 to -1.4 W m^{-2} according to several major studies (e.g., Rotstayn and Penner, 2001; Quaas et al., 2004; Ming et al., 2005). If direct and indirect sulfate radiative forcing are considered together, total climate radiative forcing is almost comparable to the warming forcing induced by greenhouse gases. Furthermore, current knowledge of sulfate amounts and distribution is imprecise; there is great uncertainty in the estimates of climate models. Further research is needed in this area and this study aims to contribute to this body of information. Simulated sulfate DRF is very sensitive to sulfate mass loading, sulfate optical properties and meteorological fields. Moreover, the biases of the simulated atmospheric state in specific atmospheric general circulation models (AGCMs) are unavoidable, which results in some regional biases in the lower troposphere that impact the radiative processes associated with the sulfate particles. One of the most important impacts is the hygroscopic increase of sulfate optical properties. Many studies (e.g., Haywood and Ramaswamy, 1998; Penner et al., 1998; Myhre et al., 2004) have indicated that uncertainty in radiative forcing of sulfate is particularly linked to hygroscopic growth and that differences in the model relative humidity (RH) fields can

cause large differences in the simulated DRF. Therefore, it is worthwhile to study issues associated with sulfate aerosols. In this study, we focused only on sulfate optical properties, their DRF, and their sensitivity to atmospheric humidity using a recent version of the State Key Laboratory of Numerical Modeling for Atmospheric Sciences and Geophysical Fluid Dynamics at the Institute of Atmospheric Physics (LASG-IAP) AGCM.

The paper is organized as follows: section 2 presents the model and its radiative scheme used in this study; section 3 presents the two different schemes for sulfate optical properties and their comparison; section 4 describes the dataset and experiment design; section 5 presents the simulation results for sulfate DRF; and section 6 summarizes the results and discusses issues for future study.

2. Model Description

2.1 AGCM used in this study

The current version of a spectral AGCM (hereinafter referred to as SAMIL, version 2.4.1) developed by LASG/IAP, is used in this study. SAMIL has 26 vertical hybrid layers and its horizontal resolution is approximately $1.67^\circ(\text{lat}) \times 2.81^\circ(\text{lon})$. The dynamical framework of SAMIL uses a "standard atmosphere reduction" scheme (Phillips, 1973) and a semi-implicit time integration (Wang et al., 2005). Large-scale cloud processes are simulated using a diagnostic scheme (Slingo, 1987). Convection processes are parameterized using the Tiedtke (1989) mass flux cumulus scheme for deep, shallow and mid-level convection, with a modified closure assumption, and allowing for the formation of organized entrainment and detrainment (Nordeng, 1994; Song, 2005; Bao et al., 2010). The land surface is simulated by the SSiB model (Xue et al., 1991; Liu and Wu, 1997). A non-local boundary layer scheme (Holtslag and Boville, 1993) and gravity-wave drag (Palmer et al., 1986) are used in SAMIL.

2.2 Radiative scheme

The radiation scheme (referred to as SES2) (Sun and Rikus, 1999a, 1999b; Sun, 2005, 2008; Li et al., 2009; Sun, 2011) used in SAMIL is modified from a radiation scheme, developed by the UK Meteorological Office (Edward and Slingo, 1996) based on the two-stream equation approach that is now used in HadCM3 (Martin et al., 2006). SES2 has nine shortwave and eight longwave spectral bands. SES2 utilizes a correlated k-distribution method (Lacis and Oinas, 1991; Fu and Liou, 1992; Mlawer et al., 1997; Li and Barker, 2005) and an updated spectral dataset. The valida-

tion study (Sun, 2011) of the line-by-line radiation model and GCM showed that SES2 can accurately simulate major gaseous absorption due to water vapor, carbon dioxide, ozone, methane, nitrous oxide, oxygen, and chlorofluorocarbons. SES2 includes many cloud optical property schemes. In the current study, we choose to use the modified Hu and Stamnes scheme (Hu and Stamnes, 1993; Sun and Rikus, 2004) and the Chou scheme (Chou, 2002) for shortwave liquid and ice clouds, respectively; the modified Hu and Stamnes scheme (Sun and Rikus, 2004) and the Slingo scheme (Slingo, 1991) for longwave liquid and ice clouds, respectively. Aerosol optical properties from the UK Meteorological Office are also included.

3. Optical properties of sulfate aerosol

The optical properties of sulfate are determined by the size distribution and refractive index (Seinfeld and Pandis, 2006). Because we use only a prescribed sulfate mass in this study, the size distribution and its parameters have to be assumed. It is well known that the hygroscopic growth effect of sulfate aerosols is important in determining its optical properties. Generally, sulfate particles are assumed to be spherical, so the Mie theory can be used to calculate the sulfate optical properties in radiative computation. The sulfate is considered as ammonium sulfate in our study.

In this study, we use two schemes for sulfate optical properties. One scheme is acquired from the UK Meteorological Office (Bellouin et al., 2007; Collins et al., 2008), and we refer it as to SR1. Another one is acquired from the work of Li et al. (2001) and Li and Min (2002); it is referred to as SR2. In both the SR1 and SR2 schemes, the Mie calculations for sulfate aerosol optical properties are performed at many single wavelengths. One band mean result in SES2 is obtained through average of the results at each individual wavelength by weighting the solar insolation. The refractive index of ammonium sulfate at selected wavelengths is taken from the work of Toon et al. (1976), but the RH growth functions used in the SR1 and SR2 schemes are different. For SR1, the sulfate accumula-

tion mode is considered because it is of most importance for aerosols (Schwartz and Andreae, 1996). The size distribution of dry sulfate has a median radius of 0.095 μm with a geometric standard deviation of 1.4. The RH growth function used in this study is based on the parameterization of Fitzgerald (1975); it consists of hygroscopic growth rates associated with 21 RH values, equally spaced from 0% to 100%. The sulfate properties are held constant when the RH is <35%. In this way, a property look-up table is predetermined and used to determine the aerosol optical properties corresponding to the RH on the model grid using linear interpolation.

For SR2, a well-recognized lognormal size distribution with a geometric mean radius of 0.05 μm and a geometric standard deviation of 2.0 is used for dry sulfate (Haywood and Ramaswamy, 1998; Penner et al., 1998; Kiehl et al., 2000). The detailed description of SR2 is shown in the appendix. Compared with many other parameterizations of sulfate properties, SR2 is simpler and more computationally efficient. It has been adopted in several climate models to study the hygroscopicity of sulfate aerosol and its radiative effects (e.g., Wang and Martin, 2007). We therefore adopt this scheme in this study as well. We have followed the parameterization procedures described in the work of Li et al. (2001) to determine the fitting coefficients for the SES2 radiative bands.

The major difference in the extinction coefficient between the SR1 and SR2 schemes occurs when RH is very close to 1.0, where sulfate is prone to be saturated and its optical properties change rapidly. In this condition, a linear interpolation with an increment of 0.05 from the look-up table of the SR1 scheme will lead to a large bias of optical properties. Generally, the sulfate optical properties are fixed, with values corresponding to RH equals to 0.99 when RH is >0.99 (Kiehl et al., 2000). In the SR2 scheme, sulfate properties are fixed to the values at RH 0.98 when RH is >0.98.

Table 1 presents the optical properties at the third shortwave band (0.50–0.625 μm) from SR1 and SR2, respectively. At low RH, the difference between the two schemes is not large, and mainly caused by different

Table 1. Specific extinction coefficient (Specific Ext, units: $\text{m}^2 \text{g}^{-1}$), single scattering albedo (SSA) and asymmetry factor from SR1 and SR2 at RH=0.0, RH=0.4, RH=0.80, and RH=0.98 in the shortwave band (0.50–0.625 μm), respectively.

RH	Specific Ext.		1-SSA (10^{-7})		Asymmetry factor	
	SR1	SR2	SR1	SR2	SR1	SR2
0.00	2.98	3.41	6.20	5.36	0.55	0.64
0.40	3.69	4.48	4.95	4.17	0.59	0.68
0.80	8.42	8.66	2.18	1.79	0.69	0.74
0.98	118.90	44.66	1.19	0.60	0.80	0.80

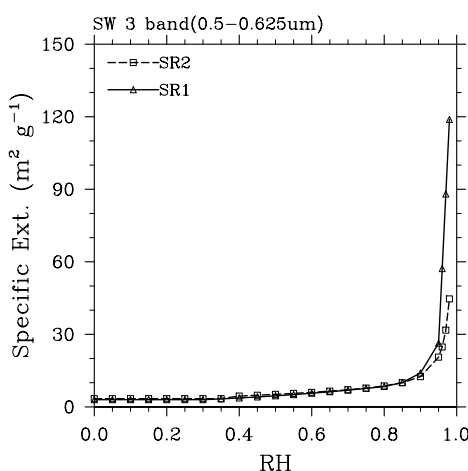


Fig. 1. The variation of specific extinction coefficient (Ext.) with RH in the third shortwave band (0.5–0.625 μm) of the SES2 radiation scheme. The triangle denotes SR1 and rectangles denote SR2.

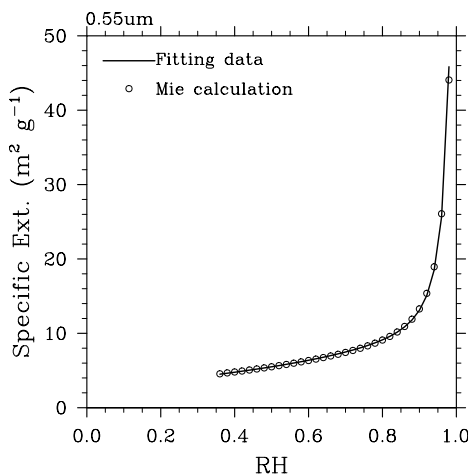


Fig. 2. The variation of specific extinction coefficient (Ext.) with RH at 0.55 μm . The circle denotes Mie calculations, with the solid line fitted to these.

size distributions. However, when RH is large the specific extinction in SR1 is much larger than that in SR2, although the single-scattering albedo (SSA) and asymmetry factors are still relatively close. Clearly, the interpolation method in SR1 is most likely responsible for overestimating the specific extinction coefficient at high RH, especially for $\text{RH} > 0.9$.

As shown in Fig. 1, the specific extinction coefficient varies smoothly and exhibits a nearly linear relation when $\text{RH} < 0.90$. When RH exceeds 0.90, the variation is very sharp; the linear interpolation method is prone to cause large biases in the SR1 scheme. Compared to SR1, the SR2 scheme parameterizes the specific extinction coefficient with a fitted expression

about RH that yields more reasonable results. The SR2 scheme is able to handle the variation of optical properties at both low and very high RH. The fitting results in SR2 match well with the Mie calculations even when RH is > 0.9 (Fig. 2). The differences between SR1 and SR2 influence the simulation of aerosol DRF in an AGCM over areas with high values of RH. The detailed effects are shown in the following sections.

When the optical properties of sulfate are available, its aerosol optical depth (AOD) can be calculated. Generally, the AOD is determined by mass extinction coefficient (β_e), aerosol mass mixing ratio (M) and the specified mass thickness path length (l). The relation can be represented by

$$\tau = M * l * \beta_e . \quad (1)$$

For the whole atmospheric column, the AOD is integrated by with the altitude. In our study, the AOD indicates the column integrated value at 0.55 μm (hereafter referred to as AOD). During our calculations, β_e is generated using the fitting equations of optical properties; the l is calculated using the vertical height and air mass density at different model layers; M is calculated from the sulfate mass mixing ratio after the re-gridding of the original NCAR CAM-Chem dataset.

4. Dataset and experiment design

4.1 Sulfate input dataset in this study

A three-dimensional monthly sulfate mass mixing ratio from NCAR CAM-Chem, which includes anthropogenic and natural sources, is used in the following AGCM simulations. The dataset is a monthly 10-year average centered around the middle of the period from 1990 to 1999. This simulation field is derived using CAM version 3.5 with a bulk aerosol model. The aerosol emissions are from the Coupled Model Inter-comparison Project Phase 5 (CMIP5) recommendation dataset (Lamarque et al., 2010), including natural and anthropogenic sources. This dataset is a good representation of the global sulfate distribution (Lamarque et al., 2011). Its spatial resolution is 1.9° (lat) $\times 2.5^\circ$ (lon) with 26 hybrid vertical levels. SAMIL adopts the same vertical hybrid coordinate coefficients as those in the NCAR CAM-Chem sulfate mass field, so only the horizontal interpolation on the SAMIL grid is performed for the original sulfate dataset.

The annual mean column-integrated sulfate loading is shown in Fig. 3. The major peaks of sulfate loading are located over Central and Eastern Europe, East Asia, Central America and Eastern United States, where the local maximum of sulfate loading is up to 15 mg m^{-2} . Other local maxima are located over

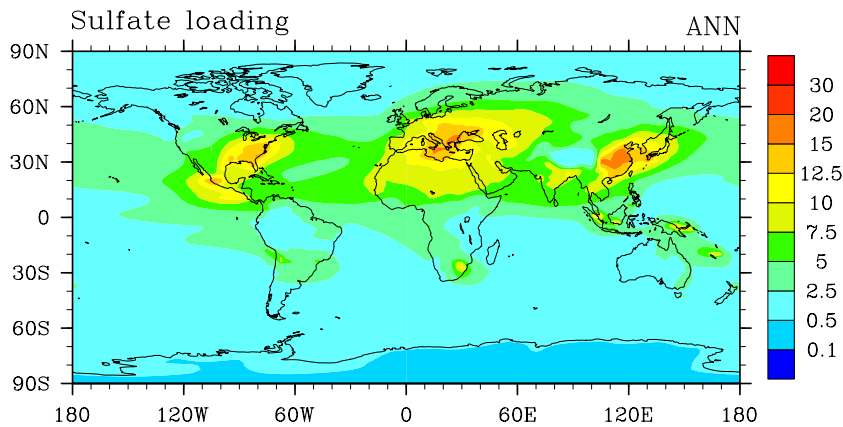


Fig. 3. Geographical distribution of the annual mean vertically integrated sulfate burden (mg m^{-2}).

Northern Australia, Northern India, Southern Africa and South America. The average global sulfate column loading is 3.44 mg m^{-2} , with an average in the Northern Hemisphere almost three times higher than that in the Southern Hemisphere. The median annual mean of sulfate loading, including natural and anthropogenic sources in aerosol comparisons between observations and models in AeroCom (<http://dataipsl.ipsl.jussieu.fr/AEROCOM/>), is 3.9 mg m^{-2} (range: 1.8 to 5.3 mg m^{-2}) (Kinne et al., 2006). Comparatively, the median annual mean of sulfate loading value in NCAR is located in the AeroCom range and exhibits a similar spatial pattern. The seasonal cycle of the zonal mean column loading (Fig. 4) also indicates that the largest sulfate loading occurs over the mid-latitudes of the Northern Hemisphere during summer, from June to August. Figure 5 shows the global average sulfate loading variation with

height. The maximum loading appears at about 1.5 km (approximately 850 hPa) of the lower troposphere and decreases rapidly with height. Because the amount of water vapor is relatively high in the lower atmosphere where RH is also within the high value range and because the specific extinction coefficient changes dramatically with RH, we expect the sulfate DRF to be very sensitive to the sulfate loading in the lower atmosphere.

To compare the sensitivity of sulfate DRF to the atmospheric humidity field, the ERA-Interim (Uppala et al., 2008) 6-hour daily specific humidity dataset from the period 1990–1999 is used to replace the predicted specific humidity in SAMIL to obtain a more realistic RH. The ERA-Interim dataset is interpolated into the SAMIL grids before calculation.

4.2 Experiment design

We use a traditional DRF definition of climate forcing at the top of the atmosphere (TOA) as employed by the Intergovernmental Panel on Climate Change (IPCC, 1995) and many researchers (e.g., Kiehl et al., 2000; Liao and Seinfeld, 2005). We consider only the change at TOA (or tropopause) for shortwave and longwave radiative fluxes due to the presence of sulfate aerosol, while holding all other climatological variables fixed. The advantage of this method is that it avoids the complexity associated with feedbacks between the altered radiation flux and the climate system dynamics. In our model, we use results at TOA because shortwave radiative transfer calculations have shown a negligible difference in the DRF calculated at the tropopause and TOA (Haywood and Shine, 1997; Forster et al., 2007). In addition, the surface forcing will be approximately the same as the DRF at TOA for scattering sulfate. Unless noted otherwise, “DRF” denotes DRF calculated at TOA in this paper.

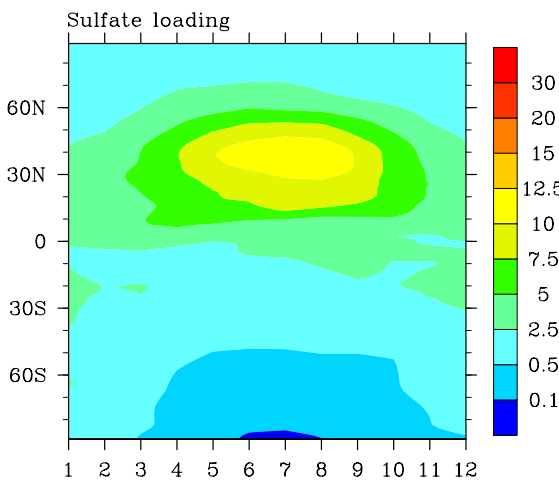


Fig. 4. Seasonal cycle of the zonal mean sulfate column loading (mg m^{-2}). Here, “1” denotes January and “12” denotes December.

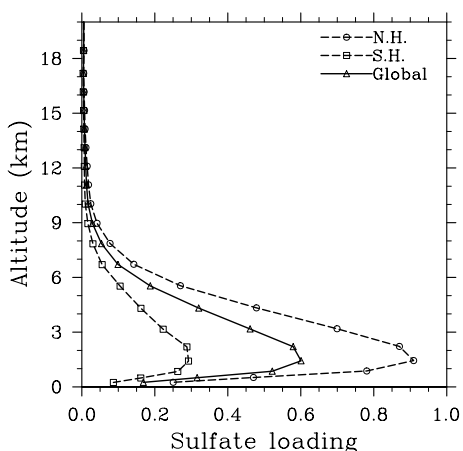


Fig. 5. Sulfate loading (mg m^{-2}) variation with height for the Northern Hemisphere (NH, circles), Southern Hemisphere (SH, rectangles), and global average (triangles).

First, we conduct a control experiment with climatological sea surface temperature and ice from the PCMDI (Program for Climate Model Diagnosis and Intercomparison), incident solar constant, and all greenhouse gases (except water vapor) kept at 1995 levels. The time step of model integration is 10 minutes for the dynamics and 3 hours for the radiative processes. When the control experiment runs to a stable state, the AGCM is integrated for a period of one year with 3-hourly output of transient variables, including air temperature, specific humidity, surface conditions, cloud water and fraction. With the 1-year transient output as input variables for the radiative process, we repeat the two DRF experiments using SAMIL with and without sulfate aerosol for 1 year. Finally, the differences between the two experiments are used to analyze monthly and annual mean calculations for the DRF results. This approach for calculating sulfate DRF is consistent with that used in the work of Kiehl et al. (2000).

5. Results

5.1 Spatial distribution of AOD and DRF

Aerosol DRF at TOA is involved in a wide range of complex climate system processes and is affected by many factors, including incident solar energy, meteorological factors, (i.e., air moisture and cloud amount), and surface albedo (Chylek and Wong, 1995). When input variables for the AGCM simulations are identical, the modeled sulfate DRF at clear-sky TOA is a good indicator of the effects of different sulfate optical properties because cloud effects are excluded.

Figure 6 shows sulfate column AOD at $0.55 \mu\text{m}$

and DRF at clear-sky TOA simulated by SAMIL with SR1 and SR2 in January. Figure 7 presents the same variables in July. Strong sulfate loading can be seen over East China, Central America, and adjacent ocean regions in January. Notably, some sulfate loading over the high-latitude ocean in the Southern Hemisphere can also be seen, mainly from natural sources (i.e., DMS and volcanic sulfate).

As shown in Figs. 6 and 7, the strong AOD and DRF are produced using the SR1 scheme in the area where sulfate loading is large. However, these values are much higher over the ocean regions adjacent to land areas with large sulfate loading. For instance, simulated AOD over some Southern Hemispheric oceans is >0.1 in January and >0.1 over the North Pacific and Atlantic oceans in July. According to the simulated sulfate loading and AOD data from the AeroCom project (Kinne et al., 2006), large sulfate loading over the Northern Hemispheric mid-latitude region generally responds to large sulfate AOD. Compared to most sulfate AOD simulated in AeroCom models, the results in Figs. 6b and 7b are not reasonable, especially over the Southern Hemisphere oceans in winter and the Northern Hemisphere oceans in summer.

These biases are mostly caused by the unreasonable moisture effect at high RH in SR1. In high-RH regions, such as the mid-latitude ocean in the Northern Hemisphere in July, overprediction due to the RH effect in SR1 scheme can easily shift the simulated peak of AOD and DRF (Figs. 7b and d). This will cause an incorrect radiative forcing and regional climate feedbacks in the climate model. In contrast to SR1, the simulation with SR2 remarkably improves the bias over high-RH regions. In the Southern Hemisphere in winter, the overestimated AOD from SR1 is distinctly reduced. In summer, the large AOD and DRF in the SR1 simulation are reduced over the ocean regions adjacent to the area with high sulfate loading, particularly in East Asia. The simulated peak of DRF is more closely connected with the center of sulfate loading than the simulation with SR1.

The global annual-mean distribution of sulfate AOD and DRF with SR2 are shown in Fig. 8. Clearly, the global pattern of sulfate DRF calculated from SR2 is more closely associated with strong sulfate loading than that associated with SR1 (figure not shown), especially over heavy industrial regions in the Northern Hemisphere. For Central and Eastern Europe (CE), East Asia (EA), and Northern America (NA), the local peak magnitude of clear-sky sulfate DRF is $>4 \text{ W m}^{-2}$ and even as great as 6 W m^{-2} in EA; the local all-sky sulfate DRF is also as much as -3 W m^{-2} . Due to cloud scattering and absorption effects, the value of

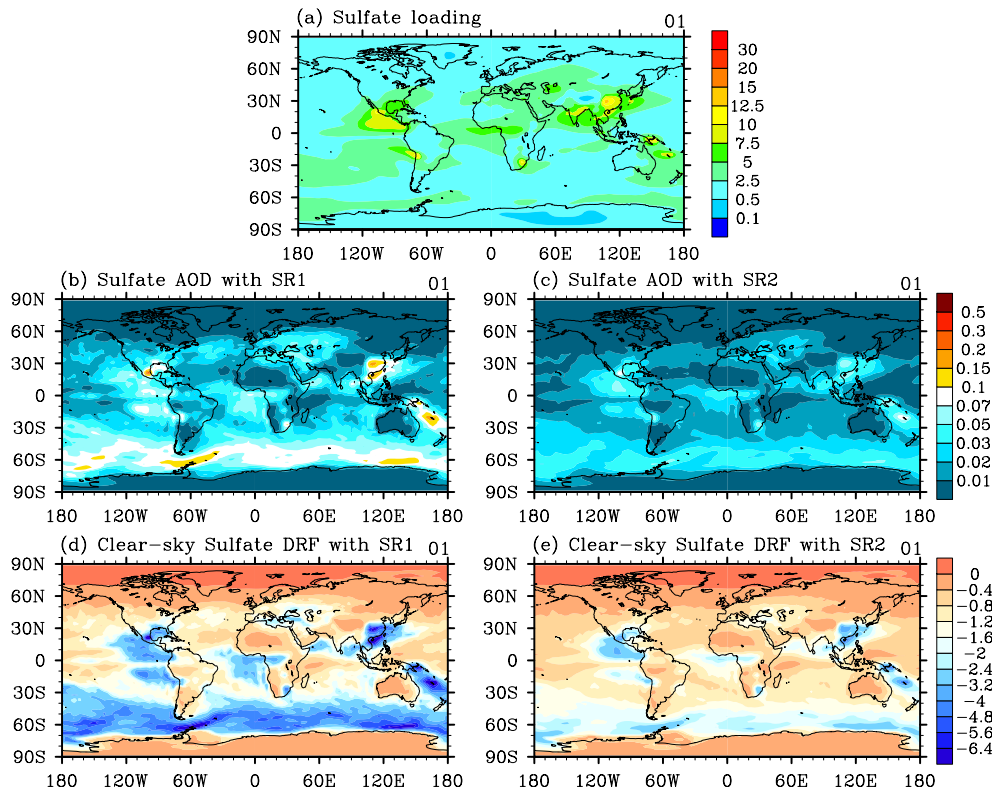


Fig. 6. Geographical distributions of sulfate (a) column burden (mg m^{-2}), (b) AOD with SR1, (c) AOD with SR2, (d) DRF (W m^{-2}) at clear-sky TOA with SR1, and (e) DRF (W m^{-2}) at clear-sky TOA with SR2 in January.

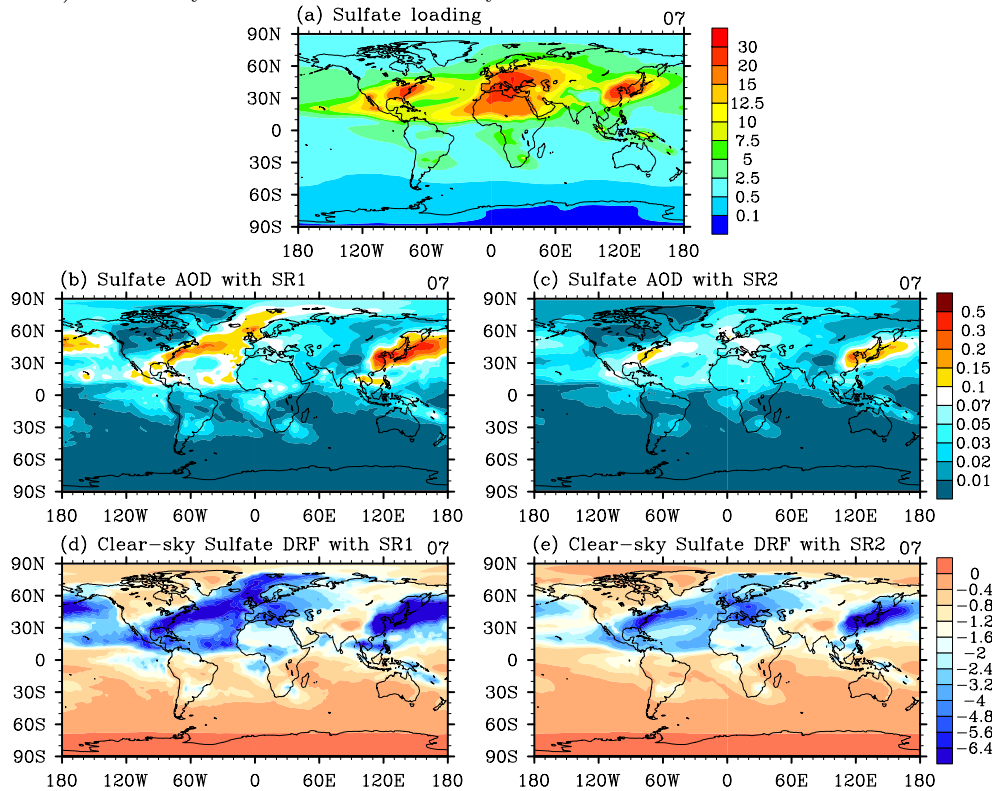


Fig. 7. Same as Fig. 6, but for July.

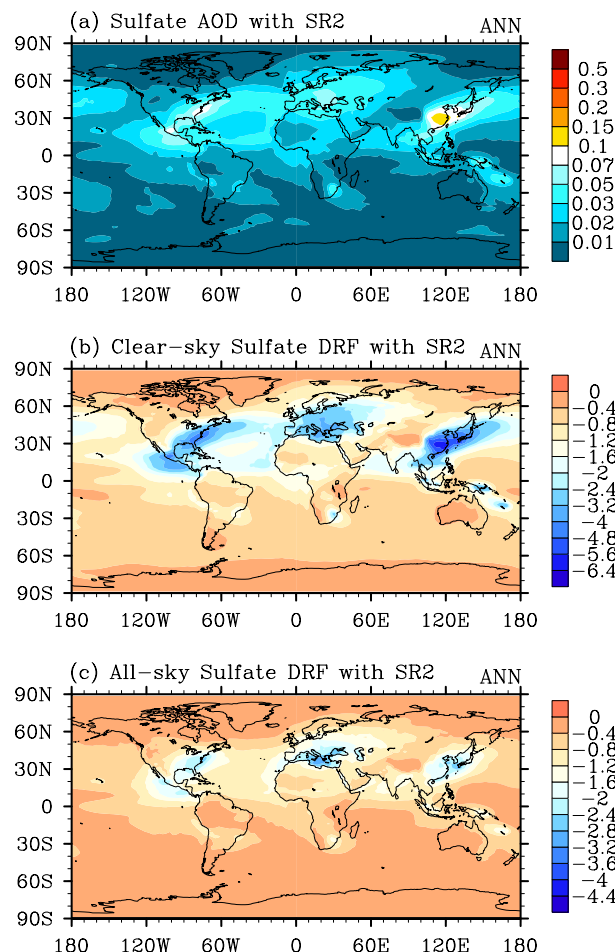


Fig. 8. Annual mean geographical distributions of sulfate (a) AOD, (b) DRF (W m^{-2}) at clear-sky TOA, and (c) DRF (W m^{-2}) at all-sky TOA with SR2 scheme.

all-sky sulfate DRF is weaker than that in clear-sky conditions, but their spatial patterns are similar. As listed in Table 2, the global average sulfate DRF in clear-sky and all-sky conditions are -1.03 and -0.57 W m^{-2} , respectively; the corresponding DRF normalized by the loading (NDRF) are -301 and -166 W g^{-1} , respectively. The DRF in the Northern Hemisphere is -1.45 W m^{-2} and -0.82 W m^{-2} for clear-sky and all-sky conditions, respectively, and the values are more than twice that in the Southern Hemisphere.

In IPCC AR4 (Forster et al., 2007), the estimated sulfate DRF is $-0.4 \pm 0.2 \text{ W m}^{-2}$. For model results participating in AeroCom project (Forster et al., 2007), the mean value of DRF is approximately -0.35 W m^{-2} with a standard deviation of 0.15 W m^{-2} and NDRF is -161 W g^{-1} . We used the total sulfate loading, which is larger than anthropogenic loading. The global annual-mean sulfate DRF and its normalized value obtained in this study are still in the range of

IPCC AR4 estimate.

5.2 Annual cycle of AOD and DRF

Figure 9 shows the annual variation of sulfate AOD, clear-sky and all-sky DRF with SR2. The modeled AOD and DRF exhibit a significant annual cycle. For the global domain and the Northern Hemisphere, the peaks occur in July. The Northern Hemisphere maximum DRF is -2.12 W m^{-2} and -1.26 W m^{-2} for clear-sky and all-sky conditions, respectively. The corresponding values of the global mean are -1.25 W m^{-2} and -0.74 W m^{-2} . Comparatively, Southern Hemisphere shows a different annual feature and its peak appears in January, mainly because of high moisture content and incident solar effects in January. On the other hand, the sulfate loading is relatively higher in January (Fig. 6a) relative to other months in the Southern Hemisphere, which also contributes to the peak of sulfate DRF in the Southern Hemisphere in winter. For the Southern Hemisphere, the maximum DRF in clear-sky and all-sky conditions are -1.18 W m^{-2} and -0.54 W m^{-2} , respectively. Sulfate loading in the Northern Hemisphere is the heaviest in July, when the average AOD and DRF are much larger than in the Southern Hemisphere. The different phases in the DRF of the two hemispheres are partially offsetting, leading to a moderate global average. These results show that the annual variation of sulfate DRF is dominated by the DRF in the Northern Hemisphere in July.

5.3 Sensitivity to air humidity bias

It is noteworthy that the global annual-mean AOD (Fig. 8a and Table 2) is <0.02 , which is weaker than many other model results (Forster et al., 2007). Furthermore, the large AOD values are not found over the European continent, where sulfate loading is high. As mentioned in previous sections, sulfate is hygroscopic, and its optical properties in an AGCM are highly related to the simulated atmospheric moisture field. Hence, the underprediction of AOD is very likely due to a dry bias in the simulated atmosphere state over Europe that occurs in the current SAMIL experiments.

Actually, compared with the air humidity from the ERA reanalysis data, the simulated low-level atmospheric humidity from SAMIL (figures not shown) is too low over most of the continents in the Northern Hemisphere. This dry bias is as much as 30%–40% in the eastern United States and Central Europe, which can very easily lead to underpredicted sulfate specific extinction. On the other hand, oceanic areas such as

Table 2. The global and hemispheric annual-mean sulfate AOD and DRF (W m^{-2}). Here, NDRF (W g^{-1}) is DRF divided by its loading.

		SH	NH	Global
AOD		0.010	0.025	0.018
DRF (W m^{-2})	Clear-sky	-0.62	-1.45	-1.03
	All-sky	-0.32	-0.82	-0.57
NDRF (W g^{-1})	Clear-sky	-352	-283	-301
	All-sky	-184	-160	-166

the western Pacific and Northern Atlantic, have large positive moisture bias, which tends to cause overprediction of sulfate specific extinction. These regions with large humidity bias are clearly linked to the bias fields of the AOD and DRF. Thus, the air humidity bias simulated in the current SAMIL experiments is a major source of the biases in radiative variables relevant to aerosol hygroscopic effects.

To further examine the relationship among simulated RH, cloud amount, and sulfate DRF, we choose three main industrial regions including CE ($35^{\circ}\text{--}50^{\circ}\text{N}$, $10^{\circ}\text{--}35^{\circ}\text{E}$), EA ($30^{\circ}\text{--}45^{\circ}\text{N}$, $100^{\circ}\text{--}125^{\circ}\text{E}$), and NA ($30^{\circ}\text{--}45^{\circ}\text{N}$, $270^{\circ}\text{--}295^{\circ}\text{E}$). The analysis period is July, when the sulfate loading is the strongest in Northern Hemisphere. The monthly sulfate DRF in each model grid is divided by its loading to normalize the value, excluding the loading effect and only emphasizing the regional difference. We use RH at the lowest model level to represent near-surface air humidity. The RH used in this analysis is calculated using the following method:

$$\text{RH} = \frac{\sum_{i=1}^{N_m} \sum_{j=1}^{N_d} q_{i,j}}{\sum_{i=1}^{N_m} \sum_{j=1}^{N_d} q_{\text{sat}(i,j)}}, \quad (2)$$

where N_m and N_d are the number of days in each month and integral steps in each day, respectively; q and q_{sat} are the specific humidity and its saturation

value in each step; and the latter is determined by simulated air temperature and pressure in model level.

Figure 10 shows the scatter distribution of sulfate normalized DRF (NDRF) in clear-sky and all-sky conditions with RH. In clear-sky conditions, the sulfate NDRF quasi-linearly varies with the simulated RH in EA and NA, whereas the ranges of NDRF are larger than that in CE. Most points in CE are concentrated in the low-RH (<0.5) domain, which is connected with large dry bias in CE. In all-sky conditions, the dependency of sulfate NDRF on RH weakens, and their variation ranges also decrease (Fig. 10b). Table 3 clearly shows that the modeled RH and cloud in CE are much lower than in EA and NA. Though the sulfate loading in CE is $\sim 40\%$ higher than in the other two regions, the lower RH and its resultant underestimation of sulfate hygroscopic effects directly lead to the lower clear-sky sulfate DRF in CE. Therefore, the largest clear-sky sulfate DRF in CE is not the largest overall, whereas the sulfate loading is the strongest over the same regions in July.

Additionally, for diagnosed cloud scheme, low RH also causes low cloud amount, which results in weak cloud scattering and absorption. Thus, the all-sky sulfate DRF is very close to its clear-sky value in CE. Similarly, due to cloud amount, the regional mean of all-sky DRF in CE is larger than that in EA and NA,

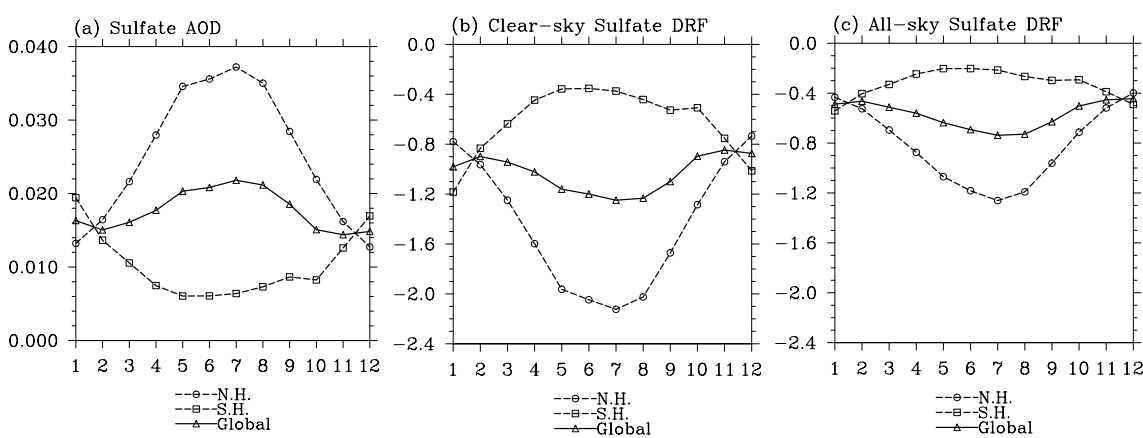


Fig. 9. Annual cycle of sulfate (a) AOD, (b) clear-sky DRF (W m^{-2}), and (c) all-sky DRF (W m^{-2}). Here, “1” denotes January and “12” denotes December.

Table 3. The regional mean of modeled RH and cloud as well as sulfate loading (mg m^{-2}), the modeled AOD and their DRF (W m^{-2}) in CE, EA, and NA. Here, the period is July; NDRF (W g^{-1}) is DRF divided by its loading.

		CE	EA	NA
RH		0.200	0.464	0.558
Total cloud		0.129	0.402	0.420
Loading (mg m^{-2})		24.86	17.41	17.96
AOD		0.069	0.108	0.090
DRF (W m^{-2})	Clear-sky	-4.73	-5.08	-5.26
	All-sky	-4.40	-2.65	-3.39
NDRF (W g^{-1})	Clear-sky	-191	-267	-289
	All-sky	-178	-152	-189

where larger cloud amount reduces the sulfate DRF. These results show that the RH effects dominate in sulfate clear-sky DRF, but cloud effects become the leading factor for all-sky DRF. Even so, sulfate DRF increases with RH in EA and NA where higher RH exists. Hence, sulfate DRF is first influenced by RH, and then their values are adjusted by regional cloud effects. These results also indicate that the features of sulfate DRF over major industrial regions are strongly influenced by their local meteorological conditions, the effects of which on DRF are even larger than that of sulfate loading. Because of great complexity of cloud simulation and their model dependency, relevant discussion is beyond the scope of this work and will be considered in future studies.

To improve these humidity biases in the SAMIL model and the resultant sulfate DRF, we replace the SAMIL-predicted specific humidity with ERA-Interim humidity data. The experimental methods are the same as mentioned previously, but the time interval is 6 h to match the time resolution of reanalysis dataset. Figure 11 shows AOD and clear-sky DRF simulated by

SAMIL running SR2 and using ERA-Interim specific humidity data in January and July, respectively. After inclusion of ERA-Interim humidity data, weaker AOD and clear-sky DRF existing in East China (Figs. 11a, c) and Central Europe (Figs. 11b, d) distinctly increase. With the reduction of moisture bias in many ocean regions, especially in the northern mid-latitude oceans, overestimation of AOD and DRF also decrease. Consequently, the annual mean of DRF is better related to the distribution of sulfate burden (Fig. 12). The global annual-mean all-sky sulfate DRF and its NDRF are -0.54 W m^{-2} and -156 W g^{-1} , respectively. Compared to the results obtained with modeled specific humidity, the clear-sky sulfate DRF increases by nearly 0.5 W m^{-2} in CE, EA and NA. Even for the all-sky DRF, its value also increases by $\sim 0.3 \text{ W m}^{-2}$ in CE and NA.

Although reanalysis humidity data from ERA-Interim is included into the model integration, the temporal resolution is still too coarse to represent the actual atmospheric humidity. Therefore, the use of reanalysis humidity data can only improve the simu-

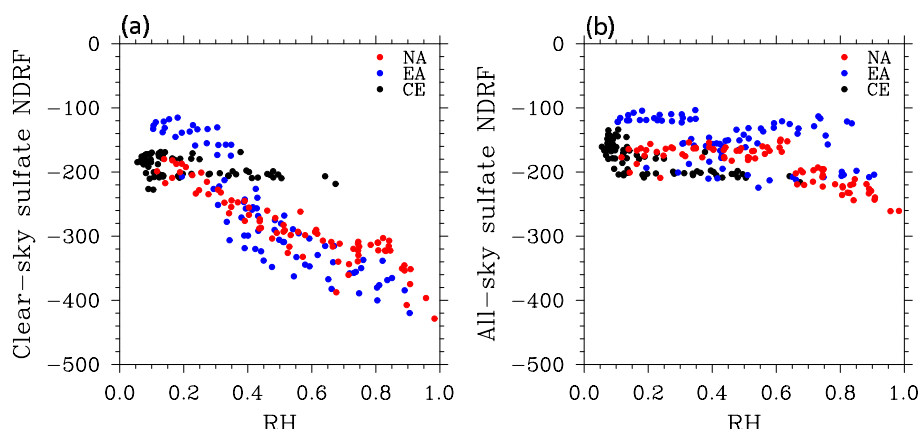


Fig. 10. Scatter distribution of sulfate normalized DRF (NDRF) (DRF divided by its sulfate loading (units: W g^{-1}) and simulated near surface RH in SAMIL over three industrial regions. (a) Clear-sky and (b) all-sky conditions, respectively. CE, EA, and NA represent central and east Europe ($10^{\circ}\text{--}35^{\circ}\text{E}$, $35^{\circ}\text{--}50^{\circ}\text{N}$), East Asia ($100^{\circ}\text{--}125^{\circ}\text{E}$, $30^{\circ}\text{--}45^{\circ}\text{N}$) and Eastern North America ($270^{\circ}\text{--}295^{\circ}\text{E}$, $30^{\circ}\text{--}45^{\circ}\text{N}$), respectively.

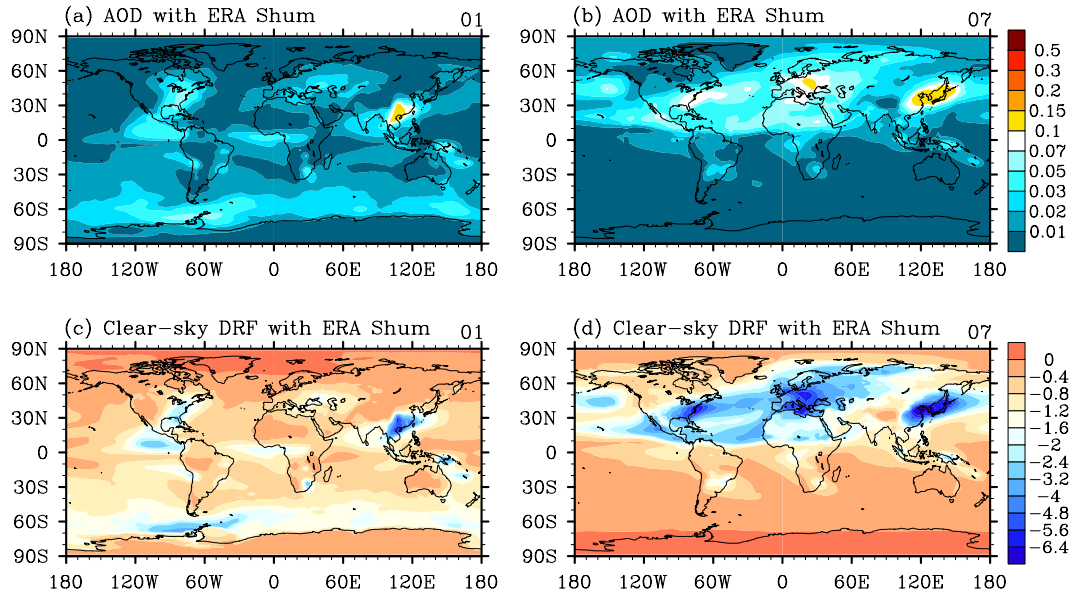


Fig. 11. Geographical distributions of sulfate AOD and DRF at clear-sky TOA (W m^{-2}) running SR2 and using ERA Interim specific humidity (Shum) data. (a) and (c) are for AOD and DRF in January, respectively; (b) and (d) are for July, respectively.

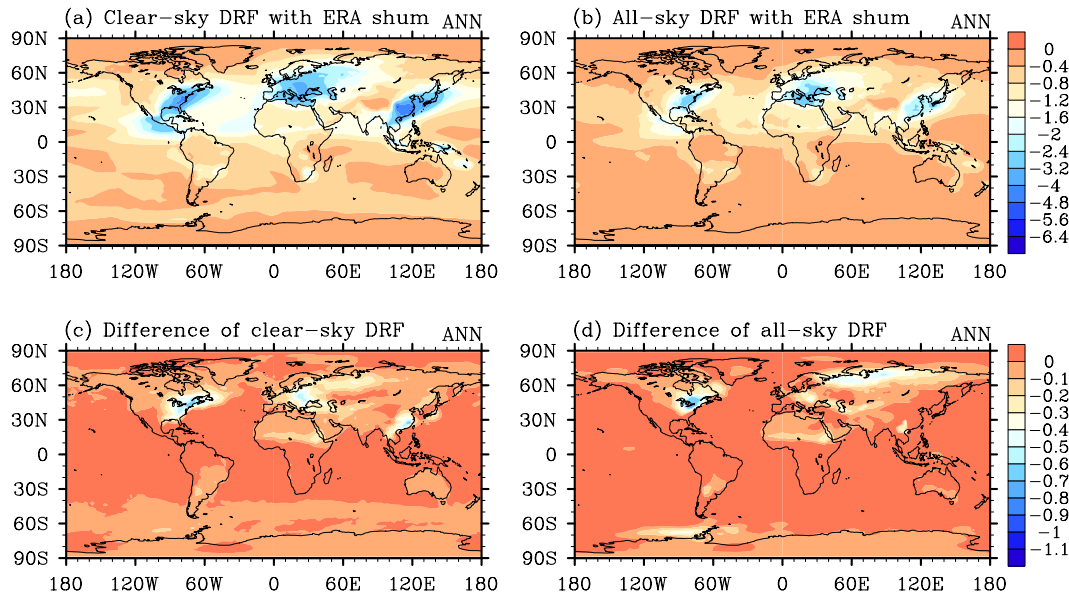


Fig. 12. Annual mean geographical distributions of sulfate DRF (W m^{-2}) and its difference running SR2 scheme and using ERA-Interim and SAMIL humidity data, respectively. (a) and (c) is for clear-sky TOA; (b) and (d) is for all-sky TOA.

lation of AOD and DRF somewhat. In addition to day biases in atmospheric moisture, the sulfate radiative properties and loading vary in different AGCMs. Compared with some other results (i.e., Penner et al. (1998), the original sulfate-specific extinction in the work of Li et al. (2001) is somewhat weaker, which is also an important reason that the simulated AOD is weaker in our study.

6. Summary and Discussion

6.1 Summary

In this study, we compare two schemes of sulfate optical properties, then a climatology monthly sulfate mass dataset is applied to calculate sulfate DRF at TOA using the meteorological fields simulated from SAMIL model.

First, the comparison of two schemes of sulfate optical properties shows that the sulfate extinction coefficient is very sensitive to RH. The sulfate hygroscopic effect on its optical properties associated with SR1 is not physically plausible, and its linear interpolation method easily leads to quite large bias of specific extinction when the RH is >0.9 . Optical properties from SR2 are calculated from a more sophisticated physical-based theory and are better able to handle sulfate hygroscopic effects. The global pattern of AOD and sulfate DRF with SR2 is closer to the sulfate loading pattern than that obtained with SR1, and SR2 distinctly reduces the overprediction seen in SR1 because of the linear interpolation. Thus, SR2 scheme is chosen for this study.

Second, the simulated local peaks of sulfate DRF occur over heavy industrial regions, and they are consistent with sulfate loading. The global annual mean sulfate DRF in clear-sky and all-sky conditions are -1.03 W m^{-2} and -0.57 W m^{-2} , respectively; the corresponding all-sky value normalized by its loading is -166 W mg^{-1} . The regional maximum all-sky DRF over Europe, East Asia, and North America is up to -4 W m^{-2} and is almost four times larger than the global average. The global annual-mean sulfate DRF in SAMIL is comparable to the ranges given in AeroCom and IPCC AR4. A distinct annual variation is seen in the modeled sulfate AOD and DRF; as for the latter, the global and Northern Hemisphere average maximums in all-sky conditions occur in July and are -0.74 W m^{-2} and -1.26 W m^{-2} , respectively. The magnitude and phase of the annual cycle are different for both hemispheres. The peak in the Southern Hemisphere appears in January.

Third, compared with the reanalysis dataset, there is a clear humidity dry bias for simulated RH over the continents in the Northern Hemisphere, especially over European regions. This directly results in a reduced sulfate hygroscopic effect, and AOD and DRF are underestimated over these regions. As for heavy industrial regions in the Northern Hemisphere, our analysis further shows that sulfate DRF is strongly affected by modeled RH and cloud amount. In clear-sky conditions, RH is the leading meteorological factor that influences local sulfate DRF over the regions above mentioned.

Finally, 6-hourly daily ERA-Interim specific humidity data is introduced into the SAMIL to replace the simulated humidity. In this experiment, the lower AOD and DRF values over the Eurasian continent are partly improved upon, and there is a tighter coupling of AOD and DRF peak locations with locations of large sulfate loading. Similarly, overpredicted AOD and DRF values over the mid-latitude ocean, adjacent

to strong sulfate-burden regions, are also decreased.

6.2 Discussion

While the impact of indirect aerosol effect has been increasingly investigated, a large degree of uncertainty remains surrounding aerosol direct effects. This is true even for essentially non-absorbing sulfate aerosols, which have been studied for a number of decades. Many factors have limited research progress. For example, current simulated aerosol-loading distributions span a wide range (Kinne et al., 2006), especially for the vertical distribution of sulfate in the lower troposphere. Additionally, sulfate size distribution, optical properties, and radiative codes often vary across models from different study groups or institutes. This diversity leads to different radiative treatments of aerosols, including sulfate. It should be especially noted that, compared to in-situ observation, the meteorology (i.e., atmospheric RH and cloud amount) and surface albedo simulated in current climate models show larger diversity and uncertainties. On the other hand, the simulation biases of meteorological field are certainly included in the calculation of sulfate DRF. All of these factors cause difficulty for the study of sulfate effects on climate.

The uncertainties noted above will impact model simulations and subsequent relevant study conclusions. This trend may be particularly challenging for full-feedback regional climate simulations over regions with a large sulfate burden, such as East Asia. Further researches are clearly required, and considerable attention should be directed at modeling the sulfate DRF and subsequent climate responses. In future work, we plan to improve humidity-related modeling processes, such as advection and cumulus convection processes, and cloud physical processes using SAMIL. With enhancement of the whole-simulation performance of SAMIL, we expect that the uncertainty of aerosol direct climate effects, i.e., sulfate optical properties and DRF, will decrease to an acceptable level for global and regional climate study.

Acknowledgements. This research is supported jointly by the grant from National Basic Research Program of China (Grant No. 2012CB955303) and from the Office of Biological and Environmental Sciences, US Department of Energy. The authors would like to thank Dr. Lamarque at NCAR for providing the sulfate mass dataset. We also thank Dr. BAO Qing in LASG/IAP for providing necessary help with running the AGCM. Dr. Gary Dietachmayer is acknowledged for reviewing and polishing the manuscript.

Table A1. In shortwave band, coefficients of fitting equations for sulfate optical properties in SES2.

SW band	λ (μm)	a_1 ($\text{m}^2 \text{ g}^{-1}$)	a_2 ($\text{m}^2 \text{ g}^{-1}$)	a_3 ($\text{m}^2 \text{ g}^{-1}$)	b_1	b_2	b_3	c_1	c_2	c_3
1	0.20–0.45	5.51	9.64×10^{-1}	1.58×10^{-1}	7.33×10^{-7}	-4.61×10^{-7}	4.19×10^{-9}	6.53×10^{-1}	1.12×10^{-1}	-1.69×10^{-3}
2	0.45–0.50	4.06	9.44×10^{-1}	7.37×10^{-2}	6.47×10^{-7}	-4.62×10^{-7}	9.35×10^{-9}	6.39×10^{-1}	1.19×10^{-1}	-2.74×10^{-3}
3	0.50–0.63	3.23	8.67×10^{-1}	3.19×10^{-2}	6.44×10^{-7}	-4.39×10^{-7}	7.80×10^{-9}	6.30×10^{-1}	1.18×10^{-1}	-3.48×10^{-3}
4	0.63–0.70	2.54	7.58×10^{-1}	-2.39×10^{-5}	6.52×10^{-7}	-3.64×10^{-7}	4.88×10^{-9}	6.17×10^{-1}	1.17×10^{-1}	-4.28×10^{-3}
5	0.70–0.83	2.07	6.78×10^{-1}	-1.84×10^{-2}	6.49×10^{-7}	2.32×10^{-7}	-1.22×10^{-8}	6.06×10^{-1}	1.53×10^{-1}	-4.89×10^{-3}
6	0.83–1.18	1.15	3.72×10^{-1}	-4.46×10^{-2}	7.36×10^{-6}	1.93×10^{-5}	-1.45×10^{-7}	5.64×10^{-1}	1.14×10^{-1}	-6.86×10^{-3}
7	1.18–1.67	5.58×10^{-1}	1.58×10^{-1}	-4.61×10^{-2}	6.60×10^{-4}	4.34×10^{-4}	1.45×10^{-5}	5.11×10^{-1}	1.09×10^{-1}	-9.07×10^{-3}
8	1.67–2.50	1.83×10^{-1}	9.05×10^{-3}	-2.70×10^{-2}	1.89×10^{-2}	-4.28×10^{-3}	4.63×10^{-4}	4.25×10^{-1}	9.84×10^{-2}	-1.25×10^{-2}
9	2.50–5.0	2.32×10^{-1}	6.66×10^{-2}	-1.67×10^{-2}	7.83×10^{-1}	-3.07×10^{-2}	1.90×10^{-2}	3.12×10^{-1}	6.99×10^{-2}	-1.41×10^{-2}

Table A2. In longwave band, coefficients of fitting equations for sulfate optical properties in SES2. The units of d_1 , d_2 and d_3 are $\text{m}^2 \text{ g}^{-1}$.

LW band	1	2	3	4	5	6	7	8
$\lambda (\mu\text{m})$	40–400	$19.23 \sim 40$	12.5–19.23	10.20–19.23	9.09–10.20	7.14–9.09	5.00–7.14	2.50–5.00
d_1	8.11×10^{-2}	1.67×10^{-3}	2.36×10^{-2}	-8.83×10^{-3}	2.57×10^{-1}	3.62×10^{-1}	3.51×10^{-1}	2.35×10^{-2}
d_2	2.26×10^{-2}	9.64×10^{-2}	1.54×10^{-1}	1.02×10^{-1}	1.77×10^{-2}	-2.34×10^{-1}	-1.79×10^{-1}	8.35×10^{-3}
d_3	8.62×10^{-4}	-3.58×10^{-3}	-7.08×10^{-3}	-4.02×10^{-3}	1.34×10^{-2}	3.58×10^{-3}	2.95×10^{-3}	-7.88×10^{-3}

APPENDIX A

SR2 scheme for sulfate optical properties

Based on the study of Li et al. (2001) study, the aerosol extinction coefficient (k_{ext}) is expressed by

$$k_{\text{ext}} = \text{WAC} * \psi, \quad (\text{A1})$$

where WAC is the wet aerosol content and ψ is the specific extinction. Both are used for wet aerosol size distributions.

$$\text{WAC} = \frac{4\pi}{3} \int \rho n(r_d)(\eta r_d)^3 dr_d, \quad (\text{A2})$$

$$\psi = \frac{\pi \int Q_{\text{ext}}(\lambda, \eta r_d)(\eta r_d)^2 n(r_d) dr_d}{\int \frac{4\pi}{3} n(r_d)(\eta r_d)^3 dr_d}. \quad (\text{A3})$$

In above equations, λ is wavelength; Q_{ext} is extinction efficiency; $n(r_d)$ represents dry aerosol size distribution; and η denotes wet aerosol particle growth factor defined as the ratio of the aerosol particle radius r at a specified RH to the radius of the corresponding dry aerosol, r_d . If we define a ratio of wet aerosol content to dry aerosol content (DAC),

$$R = \frac{\text{WAC}}{\text{DAC}}. \quad (\text{A4})$$

Equation (1) can be rewritten as

$$k_{\text{ext}} = \text{DAC} * R * \psi. \quad (\text{A5})$$

Li et al. (2001) found that R is strongly dependent on the RH but is less dependent on the effective radius of the dry aerosol size distribution. Therefore,

they proposed a parameterization of R based on average values from different effective radii of aerosol size distributions:

$$R = \exp \left(k_1 + k_2 \text{RH} + \frac{k_3}{(\text{RH} - k_4)^2} \right). \quad (\text{A6})$$

For sulfate, k_1 , k_2 , k_3 and k_4 are equal to -0.2373 , 1.135 , 0.01048 , and 1.06 , respectively. The specific extinction coefficient (ψ), asymmetry parameter (g), and single scattering albedo (ω) for each band are parameterized in the following expressions:

$$\begin{cases} \psi_i = a_{1,i} + a_{2,i} \text{RH} + \frac{a_{3,i}}{\text{RH} - 1.05} \\ 1 - \omega_i = b_{1,i} + b_{2,i} + \frac{b_{3,i}}{(\text{RH} - 1.05)} \\ g_i = c_{1,i} + c_{2,i} \text{RH} + \frac{c_{3,i}}{(\text{RH} - 1.05)} \end{cases}, \quad (\text{A7})$$

here, i denotes one shortwave band. The coefficients $a_{n,i}$, $b_{n,i}$ and $c_{n,i}$ are listed in Table A1.

For the longwave band, only sulfate absorptance (ξ) is considered, and its parameterization is

$$\xi = d_{1,i} + d_{2,i} \text{RH} + \frac{d_{3,i}}{(\text{RH} - 1.05)} \quad (\text{A8})$$

The parameterization coefficients $d_{n,i}$ are listed in Table A2. These formulas are valid when RH is < 0.98 .

REFERENCES

- Albrecht, B. A., 1989: Aerosols, cloud microphysics, and fractional cloudiness. *Science*, **245**, 1227–1230.
- Bao, Q., G. Wu, Y. Liu, J. Yang, Z. Wang, and T. Zhou, 2010: An introduction to the coupled model

- FGOALS1.1-s and its performance in East Asia. *Adv. Atmos. Sci.*, **27**, 1131–1142, doi: 10.1007/s00376-010-9177-1.
- Bellouin, N., O. Boucher., J. Haywood., C. Johnson, A. Jones, J. Rae, and S. Woodward, 2007: Improved representation of aerosols for HadGEM2. Tech. Rep., Hadley Cent. Tech. Note 73, Met Office, Exeter, UK, 43pp.
- Chou, M.-D., 2002: Parameterization of shortwave cloud optical properties for a mixture of iceparticle habits for use in atmospheric models. *J. Geophys. Res.*, **107**, doi: 10.1029/2002JD002061.
- Chylek, P., and J. Wong, 1995: Effect of absorbing aerosols on global radiation budget. *Geophys. Res. Lett.*, **22**, 929–931.
- Collins, W. J., and Coauthors, 2008: Evaluation of HadGEM2 model. Tech. Rep., Hadley Center Tech. Note 74, Met Office, Exeter, UK, 47pp
- Edwards, J. M., and A. Slingo, 1996: A studies with a flexible new radiation code. I: Choosing a configuration for a large-scale model. *Quart. J. Roy. Meteor. Soc.*, **122**, 689–719.
- Fitzgerald, J. W., 1975: Approximation fomulars for the equilibrium size of an aerosol particle as a function of its dry size and composition and the ambient relative humidity. *J. Appl. Meteor.*, **14**, 1044–1049.
- Forster, P., and Coauthors, 2007: Changes in atmospheric constituents and in radiative forcing. *Climate Change 2007: The Physical Science Basis*. Contribution of Working Group I to the Fourth Assessment Report of the Intergovernmental Panel on Climate Change, Cambridge University Press, Cambridge, United Kingdom and New York, NY, USA, 106pp.
- Fu, Q., and K. N. Liou, 1992: On the correlated k-distribution method for radiative transfer in nonhomogeneous atmospheres. *J. Atmos. Sci.*, **49**, 2139–2156.
- Haywood, J. M., and K. P. Shine, 1997: Multi-spectral calculations of the direct radiative forcing of tropospheric sulphate and soot aerosols using a column model. *Quart. J. Roy. Meteor. Soc.*, **123**, 1907–1930.
- Haywood, J. M., and V. Ramaswamy, 1998: Global sensitivity studies of the direct radiative forcing due to anthropogenic sulphate and black carbon aerosols. *J. Geophys. Res.*, **103**, 6043–6058.
- Holtslag, A. M., and Boville, B. A. 1993: Local versus nonlocal boundary-layer diffusion in a global climate model. *J. Climate*, **6**, 1825–1842.
- Hu, Y. X., and K. Stamnes, 1993: An accurate parameterization of the radiative properties of water clouds suitable for use in climate models. *J. Climate*, **6**, 728–742
- IPCC, 1995: *Climate Change 1995: The Science of Climate Change*. J. T. Houghton et al., Eds., Cambridge Univ. Press, New York, 1996, 572pp.
- Kiehl, J. T., and B. P. Briegleb, 1993: The relative roles of sulfate aerosols and greenhouse gases in climate forcing. *Science*, **260**, 311–314.
- Kiehl, J. T., T. L. Schneider, P. J. Rasch, M. C. Barth, and J. Wong, 2000: Radiative forcing due to sulfate aerosols from simulations with the National Center for Atmospheric Research Community Climate Model, Version 3. *J. Geophys. Res.*, **105**(D1), 1441–1457.
- Kinne, S., and Coauthors, 2006: An AeroCom initial assessment—Optical properties in aerosol component modules of global models. *Atmos. Chem. Phys.*, **5**, 8285–8330.
- Lacis, A. A., and V. Oinas, 1991: A description of the correlated k-distributed method for modeling nongray gaseous absorption, thermal emission, and multiple scattering in vertically inhomogeneous atmospheres. *J. Geophys. Res.*, **96**, 9027–9063, doi: 10.1029/90JD01945.
- Lamarque, J. F., and Coauthors, 2010: Historical (1850–2000) gridded anthropogenic and biomass burning emissions of reactive gases and aerosols: Methodology and application. *Atmos. Chem. Phys.*, **10**, 7017–7039.
- Lamarque, J. F., and Coauthors, 2011: Global and regional evolution of short-lived radiatively-active gases and aerosols in the Representative Concentration Pathways. *Climatic Change*, **109**, 191–212.
- Liao, H., and J. H. Seinfeld, 2005: Global impacts of gas-phase chemistry-aerosol interactions on direct radiative forcing by anthropogenic aerosols and ozone. *J. Geophys. Res.*, **110**, (D18208), doi: 10.1029/2005JD005907.
- Li, J., and Q. Min, 2002: Parameterization of the optical properties of sulfate aerosols in the infrared. *J. Atmos. Sci.*, **59**, 3130–3140.
- Li, J., and H. W. Barker, 2005: A radiation algorithm with correlated k-distribution. Part I: Local thermal equilibrium. *J. Atmos. Sci.*, **62**, 286–309.
- Li, J., J. G. D. Wong, J. S. Dobbie, and P. Chylek, 2001: Parameterization of the optical properties and growth of sulfate aerosols. *J. Atmos. Sci.*, **58**, 193–209.
- Li, J., Y. Liu, Z. Sun, and G. Wu, 2009: The impacts of the radiation and cumulus convective parameterization on the radiation fluxes in SAMIL. *Acta Meteorologica Sinica*, **673**, 355–369. (in Chinese)
- Liu, H., and G. Wu, 1997: Impacts of land surface on climate of July and onset of summer monsoon: A study with an AGCM plus SSIB. *Adv. Atmos. Sci.*, **14**, 289–308.
- Lohmann, U., J. Feichter, C. C. Chuang and J. E. Penner, 1999: Prediction of the number of cloud droplets in the ECHAM GCM. *J. Geophys. Res.*, **104**, 9169–9198.
- Martin, G. M., M. A. Ringer, V. D. Pope, A. Jones, C. Dearden, and T. J. Hinton, 2006: The physical properties of the atmosphere in the new Hadley Centre Global Environmental Model, HadGEM1. Part 1: Model description and global climatology. *J. Climate*, **19**, 1274–1301.
- Ming, Y., V. Ramaswamy, P. A. Ginoux, L. W. Horowitz, and L. M. Russell, 2005: Geophysical Fluid Dynam-

- ics Laboratory general circulation model investigation of the indirect radiative effects of anthropogenic sulfate aerosol. *J. Geophys. Res.*, **110**(D22206), doi: 10.1029/2005JD006161.
- Mlawer, E. J., S. J. Taubman, P. D. Brown, M. J. Iacono, and S. A. Clough, 1997: Radiative transfer for inhomogeneous atmospheres: RRTM, a validated correlated- k model for the longwave. *J. Geophys. Res.*, **102**, 16663–16682.
- Myhre, G., F. Stordal, T. F. Berglen, J. K. Sundet, and I. S. A. Isakesen, 2004: Uncertainties in the radiative forcing due to sulfate aerosols. *J. Atmos. Sci.*, **61**, 485–498.
- Nordeng, T. E., 1994: Extended versions of the convective parameterization scheme at ECMWF and their impact on the mean and transient activity of the model in the tropics. ECMWF Technical Memo. 206, Reading, England, 41pp.
- Palmer, T. N., G. J. Shutts, and R. Swinbank, 1986: Alleviation of a systematic westerly bias in general circulation and numerical weather prediction models through an orographic gravity wave drag parameterization. *Quart. J. Roy. Meteor. Soc.*, **112**, 1001–1039.
- Penner, J. E., C. C. Chuang, and K. Grant, 1998: Climate forcing by carbonaceous and sulphate aerosols. *Climate Dyn.*, **14**, 839–851.
- Phillips, N. A., 1973: Principles of large-scale numerical weather prediction. *Dynamic Meteorology*, Morel and Reidel, Eds., Dordrecht, Holland, 1–96.
- Quaas, J., O. Boucher, and F.-M. Breon, 2004: Aerosol indirect effects in POLDER satellite data and the Laboratoire de Météorologie Dynamique-Zoom (LMDZ) general circulation model. *J. Geophys. Res.*, **109**(D08205), doi: 10.1029/2003JD004317.
- Ramaswamy, V., and Coauthors, 2001: Radiative forcing of climate change. *Climate Change 2001: The Scientific Basis*. Contribution of Working Group I to the Third Assessment Report of the Intergovernmental Panel on Climate Change. Houghton et al., Eds. Cambridge University Press, Cambridge, United Kingdom and New York, NY, USA, 349–416.
- Rotstayn, L. D., and J. E. Penner, 2001: Indirect aerosol forcing, quasi forcing, and climate response. *J. Climate*, **14**, 2960–2975.
- Schwartz, S. E., and M. O. Andreae, 1996: Uncertainty in climate change caused by aerosols. *Science*, **272**, 1121–1122.
- Seinfeld, J. H., and S. N. Pandis, 2006: *Atmospheric Chemistry and Physics: From Air Pollution to Climate Change*. 2nd ed., J. Wiley, New York, 1231pp.
- Slingo, A., 1991: A simple parametrization for the radiative properties of ice clouds. Report of Fourth ICE/EUCREX Workshop, 190–198.
- Slingo, J. M., 1987: The development and verification of a cloud prediction scheme for the ECMWF model. *Quart. J. Roy. Meteor. Soc.*, **113**, 899–927.
- Song, X. L., 2005: The evaluation analysis of two kinds of mass flux cumulus parameterizations in climate simulation. Ph. D. dissertation, Institute of Atmospheric Physics, Chinese Academy of Sciences, 155pp. (in Chinese)
- Sun, Z., 2005: Parameterizations of radiation and cloud optical properties. BMRC Research Report, 107–112.
- Sun, Z., 2008: Development of the Sun-Edwards-Slingo radiation scheme (SES2), The Centre for Australian Weather and Climate Research (CAWCR) Technical Report No. 009, 94pp.
- Sun, Z. 2011: Improving transmission calculations for the Edwards-Slingo radiation scheme using a correlated- k distribution method. *Quart. J. Roy. Meteor. Soc.*, **137**, 2138–2148.
- Sun, Z., and L. Rikus, 1999a: Improved application of exponential sum fitting transmissions to inhomogeneous atmosphere. *J. Geophys. Res.*, **104**, 6291–6303.
- Sun, Z., and L. Rikus, 1999b: Parameterization of effective radius of cirrus clouds and its verification against observations. *Quart. J. Roy. Meteor. Soc.*, **125**, 3037–3056.
- Sun, Z., and L. Rikus, 2004: Validating model clouds and their optical properties using geostationary satellite imagery. *Mon. Wea. Rev.*, **132**, 2006–2020.
- Tiedtke, M., 1989: A comprehensive mass flux scheme for cumulus parameterization in large-scale models. *Mon. Wea. Rev.*, **117**, 1779–1800.
- Toon, O. B., J. B. Pollack, and B. N. Khare, 1976: The optical constants of several atmospheric aerosol species: Ammonium sulfate, ammonium oxide and sodium chloride. *J. Geophys. Res.*, **81**, 5733–5748.
- Twomey, S., 1977: The influence of pollution on the short-wave albedo of clouds. *J. Atmos. Sci.*, **34**, 1149–1152.
- Uppala, S., D. Dee, S. Kobayashi, P. Berrisford, and A. Simmons, 2008: Towards a climate data assimilation system: Status update of ERA-Interim. European Centre for Medium-Range Weather Forecasts (ECMWF), Newsletter, No. 115, 12–18.
- Wang, Z. Z., G. X. Wu, P. Liu, and T. W. Wu, 2005: The development of GOALS/LASG AGCM and its global climatological features in climate simulation. I—Influence of horizontal resolution. *Journal of Tropical Meteorology*, **21**, 225–237. (in Chinese)
- Wang, J., and S. T. Martin, 2007: Satellite characterization of urban aerosols: Importance of including hygroscopicity and mixing state in the retrieval algorithms. *J. Geophys. Res.*, **112**(D17203), doi: 10.1029/2006JD008078
- Xue, Y., P. J. Sellers, J. L. Kinter, and J. Shukla, 1991: A simplified biosphere model for global climate studies. *J. Climate*, **4**, 345–364.